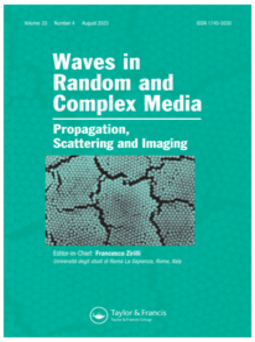

Taylor & Francis
Taylor & Francis Group

Waves in Random and Complex Media

ISSN: (Print) (Online) Journal homepage: https://www.tandfonline.com/loi/twrm20

Theoretical study of a Janus layered photonic structures based on improved particle swarm algorithm for detection of serum creatinine and glucose concentration

Jie Xu, Zhao Tang, You-ran Wu & Hai-feng Zhang

To cite this article: Jie Xu, Zhao Tang, You-ran Wu & Hai-feng Zhang (20 Sep 2023): Theoretical study of a Janus layered photonic structures based on improved particle swarm algorithm for detection of serum creatinine and glucose concentration, Waves in Random and Complex Media, DOI: 10.1080/17455030.2023.2259501

To link to this article: https://doi.org/10.1080/17455030.2023.2259501

Published online: 20 Sep 2023.

WAVES IN RANDOM AND COMPLEX MEDIA
https://doi.org/10.1080/17455030.2023.2259501

Taylor & Francis
Taylor & Francis Group

Theoretical study of a Janus layered photonic structures based on improved particle swarm algorithm for detection of serum creatinine and glucose concentration

Jie Xu[a], Zhao Tang[b], You-ran Wu[b] and Hai-feng Zhang[b]

[a]College of Electronic and Optical Engineering & College of Flexible Electronics (Future Technology), Nanjing University of Posts and Telecommunications, Nanjing, People's Republic of China; [b]Bell Honors School & Intensive Courses in Science and Engineering, Nanjing University of Posts and Telecommunications, Nanjing, People's Republic of China

ABSTRACT

An improved particle swarm optimization (IPSO) algorithm is proposed to perform parameter optimization of the sensor which is realized by Janus layered photonic structures (LPS) based on the optical Tamm state (OTS) and defect layer, which can be used to detect serum creatinine (SCR) solution concentration (C_{SCR}) and glucose solution concentration (C_G) by adjusting the thickness and refractive index (RI) of the medium in the structure to control the peak and frequency changes of the transmission and absorption peaks. Due to the characteristic of Janus, the light incident from different directions can produce different effects. The OTS based on metal properties has sensitive and narrow absorption peaks when the light comes in forward propagation, its absorption characteristics allowing accurate measurement of C_{SCR} with a high sensitivity (S) of 172 THz/RIU and a relevant quality factor (Q) of 651 and a lower detection limit (DL) of 2.3163×10^{-4}. It has a significant Q of 4.5×10^4, DL of 4.825×10^{-5}, and S of 11.7857 THz/RIU with its transmission characteristics which can be used to detect C_G when the light comes in backward propagation. It can be said that the IPSO has a certain application prospect for the design of optical sensing.

ARTICLE HISTORY
Received 10 January 2023
Accepted 11 September 2023

KEYWORDS
Improved particle swarm optimization algorithm; optical Tamm state; refractive index sensing; Janus metastructure; layered photonic structures

1. Introduction

In 1987, Yablonovitch and John each introduced the concept of 'photonic crystals' when they studied the relationship between light propagation behavior and periodic dielectric structure in materials [1,2]. Layered photonic structures (LPS) have some unique physical properties such as photonic band gap and energy localization [3,4]. In recent years, LPS have developed rapidly, and based on these unique characteristics have been proposed to make optical sensors that can detect various physical quantities, such as cancer cells, temperature, and low refractive index (RI) [5–7]. LPS can be used to make sensors based on

CONTACT Hai-feng Zhang hanlor@163.com, hanlor@njupt.edu.cn

different principles due to their unique physical properties, appropriate absorption, transmittance, and high sensitivity (*S*) levels caused by the sparking visual quality displayed over a certain wavelength range [8,9].

LPS can be easily prepared in very small sizes which meet the size requirements of the sensors [10].

Many longitudinal studies found that diverse configurations based on the LPS have shown relevant advantages in lots of fields. Most research can only realize the physical sensing of electromagnetic wave incidence in one direction. This paper achieves the purpose of bidirectional measurement through Janus, on behalf of the Roman god of creation who has two faces looking into the past and the future. The two-sided nature of Janus provides the structure with impropriety and direction so that Janus holds diverse attributes and functions, for example, quantum property and molecular sensing [11,12], which are incompatible when in the common structures without Janus, thus providing more possibilities for building multifunctional physical structures [13]. It is due to the unique physical properties of Janus that it is possible to achieve multiple physical quantities and multifunctional measurements on the same structure during the design of the sensor. When light enters from different directions, Janus performs its general purpose, allowing the physical structure to exhibit different transmittance, absorption, and reflectance. This is very efficient and beneficial in practical application. The multifunctional sensor design defines a single sensor with the ability to perform the functions of multiple sensors. This is achieved through the use of a unique structure that exhibits varying resolution and sensing principles based on the direction of incident light, both before and after it passes through the structure. These differences in the light's behavior allow for measurement in different detection ranges, ultimately resulting in the multifunctional capabilities of the sensor.

Glucose and serum creatinine (SCR) are essential components in the human body, and the content of glucose in the human body reacts to life and health [14], and hyperglycemia has long been one of the common human diseases. Therefore, the accurate detection of glucose concentration (C_G) has a great impact on the food life and physical health of humans [15]. In 2017, Su et al. then used a glucose sensor with an electrochemical signal transducer [16]. SCR is one of the most vital indicators to detect the human body, both for diabetes and for the determination of kidney function, which is very dependent on the SCR concentration (C_{SCR}) [17]. The Jaffé reaction kinetic method or endpoint method is the predominant method of detection in previous research.

LPS is widely used in sensor measurement, but most of the current research is limited to unidirectional measurement or bidirectional measurement with similar properties. In this paper, with the help of particle swarm optimization (PSO), the sensor measurement based on transmission and absorption can be realized in the LPS with Janus metastructure, which has this outstanding function but also can maintain excellent sensitivity (*S*) and other sensing properties. To computationally compare the excellence of different structures, the neural network transfer matrix method (TMM) has been provided in previous studies to build LPS and solve for absorptivity and transmittance [18,19]. The optimization algorithm can speed up the calculation of the TMM and seek the appropriate parameters thus building a superior structure. PSO is first proposed by Kennedy et al. [20] has attracted the attention of researchers because of its simple principle, and fast convergence, and has become one of the most popular optimization algorithms [21]. In a bid to apply the original PSO algorithm to the high-dimensional matrix operations of the transfer matrix and to perform as many iterations of the optimization as possible, this section improves on the original version of the PSO algorithm [22]. The purpose of PSO is to find the global optimal solution automatically, compared to the primitive method which uses enumeration to plug in different values, simulation efficiency can be improved to save time, and more excellent transmission and absorption curves can be obtained to improve *S* and quality factors (*Q*). Slightly superior results are achieved with improved PSO helps to construct excellent LPS. However, like any other device, Janus sensors are not immune to design defects that can impact their performance. One potential limitation of Janus sensors is their narrowband frequency range, which may restrict their ability to detect changes in the refractive index outside of this range. Additionally, the Janus sensor may exhibit nonlinear behavior due to the interaction between light and the metamaterial structure, which can introduce hysteresis or other nonlinear effects that may compromise the accuracy and stability of the sensor. Currently, these issues have not been fully addressed in the existing research work.

In this paper, an OTS-based Janus sensor is proposed. Two cavities of different sizes for a degree of deformation, RI, and biomass are designed by constructing a suitable LPS when light is incident from different directions. In the measurement of SCR and glucose, the positions of analytes 1 and 2 (see Figure 1) are placed into the lumen. The measurement range of C_{SCR} concentration is 80.9$\sim$85.28 μmol L^{-1} (RI of 2.565$\sim$2.661), and the corresponding *S* of 172 THz/RIU can be obtained from the results. A relevant *Q* of 651, a figure of merit (*FOM*) of 216, and a detection limit (*DL*) of 2.3163×10^{-4}, respectively. When C_G is measured, the position of analyte 1 is placed with a common medium with a corresponding concentration range of 4%$\sim$84.1% (RI of 1.34$\sim$1.48), S = 11.7857 THz/RIU, $Q = 4.5 \times 10^4$, $FOM = 1.1 \times 10^3$, and $DL = 4.825 \times 10^{-5}$. In the thickness and RI detection, it also has excellent performance. Accurate assignment of this designed LPS based on the Janus property can be a very useful and sophisticated optical sensor, which performs relevant measurements of multiple physical quantities. This proposed unique sensing structure has a certain prospect in the field of muti-physical quantity measurement.

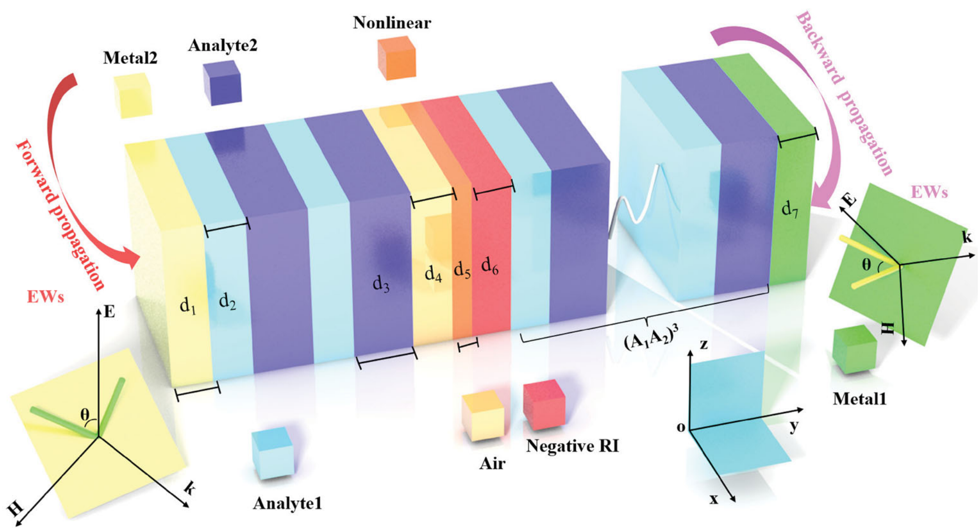

Figure 1. The structure atlas of Janus LPS.

2. Theoretical model

2.1. Basic models

The proposed Janus LPS which is a multifunctional new sensing structure consisting of 15 layered structures that can measure both C_G and C_{SCR} is plotted in Figure 1. The structure is denoted as $M_2(A_1A_2)^2BNC(A_1A_2)^3M_1$, where M_1 and M_2 refer to the metal Argentum (Ag) layers that are used to excite the optical Tamm state (OTS). The dielectric constant model equation for the OTS can be expressed as follows [23]:

$$\varepsilon_{Ag} = E_{00} - \omega_{Ag}{}^2/(j \times \omega_p \times r_m + \omega_p{}^2) - Z \times O_{Ag}{}^2/(\omega_p{}^2 - O_{Ag}{}^2 + j \times F_{Ag}), j = \sqrt{-1}$$

In this expression, $E_{00} = 2.4064$ and $Z = 1.6604$ stand for the dielectric constant and RI of the initial Ag layer, w_{Ag}, O_{Ag}, F_{Ag} and r_m respectively denotes the angular frequency of $4.428\pi \times 10^{15}$, $2.66\pi \times 10^{15}$, $1.24\pi \times 10^{15}$ and $9.6\pi \times 10^{12}$, where w_p represents the current operating frequency. EWs represent the electromagnetic wave. And $d_1 \sim d_7$ stands for the dimensions of different layered structures separately. A_1 and A_2 are analyte layers, the thickness of which are 69.3 and 31.5 nm. B is an air layer with $d_4 = 65.2$ nm, and C is a negative RI layer with $n = -2.2$, $d_6 = 185$ nm [24]. N is a polystyrene layer which used as a defect layer to realize the sensing function of LPS. And when this study uses polystyrene as a nonlinear material, it should set third-order nonlinear susceptibility (x_3) of 1.14×10^{-12} and the ambient light intensity (It) is 70,000 lx [25]. The calculation of dielectric constant and RI is different when the nonlinear material is added to LPS which indicates as

$$E_i = \sqrt{It \times 2/(c \times E_0)}$$

where $E_0 = 8.854 \times 10^{-12}$ denotes electric permittivity in a vacuum and $c = 3 \times 10^8$ stands for the speed of light. And the expression of nonlinear RI is [26]

$$n_N = n_0 + (x_3/(2 \times n_0)) \times |E|^2$$

where n_0 represents the linear RI of nonlinear material and E denotes the output electrokinetic rate of the layered structure before the nonlinear layer. The optical properties of SCR and glucose are mentioned in previously reported studies, thus allowing the introduction of LPS in the visible wavelength band in the layered structures [27–29]. On account of the non-reciprocal transmission properties, we think of SCR as an analyte 1 and normal media with $n = 2.9$ as analyte 2 when the structure used to assay C_{SCR}. We fill the glucose solution to the position of analyte 2 and normal media with $n = 1.4$ to the position of analyte 1 when we assay C_G.

2.2. Calculation method

2.2.1. TMM

A transverse electric (TE) wave, in which there is no electric field component in the direction of propagation perpendicular to the surface of the medium, is incident at an angle of twenty degrees along the vertical direction of the medium's surface. The wave is analyzed using the transfer matrix method (TMM) to investigate its transmission through different media. The details of the analysis are as follows. When light is incident, the electromagnetic wave signal propagates from the surface of the designed LPS. There is no electric field component in the propagation direction of the structure, but there is a magnetic field component that is perpendicular to it. The structure has this physical property no matter which direction it enters from.

The physical conclusions presented by Maxwell's set of equations, and then based on the transmission boundary conditions of the magnetic and electric fields, are deduced to derive the equations of the electric and magnetic fields in the iterative process, and the solution yields the transmission characteristics and dispersion relations of the LPS [30].

For the *u*th single layer, the recursive matrix equation for the electric and magnetic field relations in the proposed LPS can be written as [31]

$$\begin{pmatrix} \frac{E_u}{H_u} \end{pmatrix} = M \begin{pmatrix} \frac{E_{u+1}}{H_{u+1}} \end{pmatrix} \tag{1}$$

In the TE mode, the transfer matrix in the normal dielectric layer is [31]

$$M_u^{TE} = \begin{pmatrix} \cos(k_{uz}d_u) & -\frac{j}{\eta_u^{TE}}\sin(k_{uz}d_u) \\ -j\eta_u^{TE}\sin(k_{uz}d_u) & \cos(k_{uz}d_u) \end{pmatrix} \tag{2}$$

Its $k_{uz} = k_u cos\theta$, $k_u = \sqrt{\varepsilon_u}\omega/c$, $\eta_u^{TE} = \sqrt{\varepsilon_0/\mu_0}\sqrt{\varepsilon_u}\cos\theta_u$, where d_u stands for the thickness of the *u*th layer, ε_u on behalf of the dielectric constant of the *u*th layer. According to Snell's law of refraction, $\theta_u = \arcsin(n_0\sin(\theta_0)/n_u)$, where n_0 is the RI of the medium in where the light comes in, n_u is the RI of the medium in which the *u*th layer is located, and θ_0 is the angle of incidence from the air into the structure.

The whole LPS consists of several layered structures, the connections of each layer follow the same transport matrix equation, so the overall structure can be represented by a matrix equation as follows.

$$M = \sum_{j=1}^{U} M_j = \begin{pmatrix} M_{11} & M_{12} \\ M_{21} & M_{22} \end{pmatrix} \tag{3}$$

While the transfer matrix in the normal nodal layer is very different from the nonlinear layer structure [32], after knowing the electric field at the back interface of the entire nonlinear medium, a layer of the photonic structure is divided into multiple layers equally, and then from back to front, the nonlinear transfer matrix equations can be derived for the front and back interfaces of the nonlinear medium step by step.

$$\begin{pmatrix} \frac{E_u}{H_u} \end{pmatrix} = O_1O_2O_3\cdots O_m = O_D \begin{pmatrix} \frac{E_{m+1}}{H_{m+1}} \end{pmatrix} \tag{4}$$

$$M = O_BO_DO_R \tag{5}$$

where O_B and O_D are the transfer matrices relatively derived from the front and back interfaces of the nonlinear medium.

The coefficient of reflection (r) and coefficient of transmission (t) are calculated in this way, and the equations can be expressed as

$$r = \frac{(M_{11} + M_{12}\eta_{U+1})\eta_0 - M_{21} - M_{22}\eta_{U+1}}{(M_{11} + M_{12}\eta_{U+1})\eta_0 + M_{21} + M_{22}\eta_{U+1}} \tag{6}$$

$$t = \frac{2\eta_0}{(M_{11} + M_{12}\eta_{U+1})\eta_0 + M_{21} + M_{22}\eta_{U+1}} \tag{7}$$

The equations for reflectance (R), transmittance (T) and absorbance (A) are $R = r \cdot r^*$, $T = t \cdot t^*$, $A = 1 - T - R$, where r^* and t^* are on behalf of the conjugate values of r and t, respectively.

2.2.2. IPSO method

The PSO for multi-objective optimization has been a very common reference, assuming that the number of parameters to be optimized is w, which means that the matrix of stored particles is a w-dimensional matrix. The w-dimensional space can be imagined as a multi-dimensional space, and the coordinates of each particle in the space are the objective function that is adjusted to obtain the optimal solution. The basic process of the PSO and the application of the relevant calculation formula are given below [33]. This formula is the iterative formula for the particle position and velocity vectors. Figure 2 shows the algorithm process and the ways of calculation.

$$\begin{cases} X_{k+1}(w) = X_k(w) + V_k(w) \\ V_{k+1}(w+1) = iV_k(w) + \sum\limits_{p_i \in N_k} c_i r_i (P_i(w) - X_k(w)) \end{cases} \\ w = 1, 2, \ldots, W_F, k = 0, 1, 2..D \tag{8}$$

where W_F uses to describe the number of particle swarms and D denotes the number of iterations. *X(w)* stands for the position of the particle, *V(w)* on behalf of the directional velocity vector, and *P(w)* is used to store the optimal positions and can be divided into individual

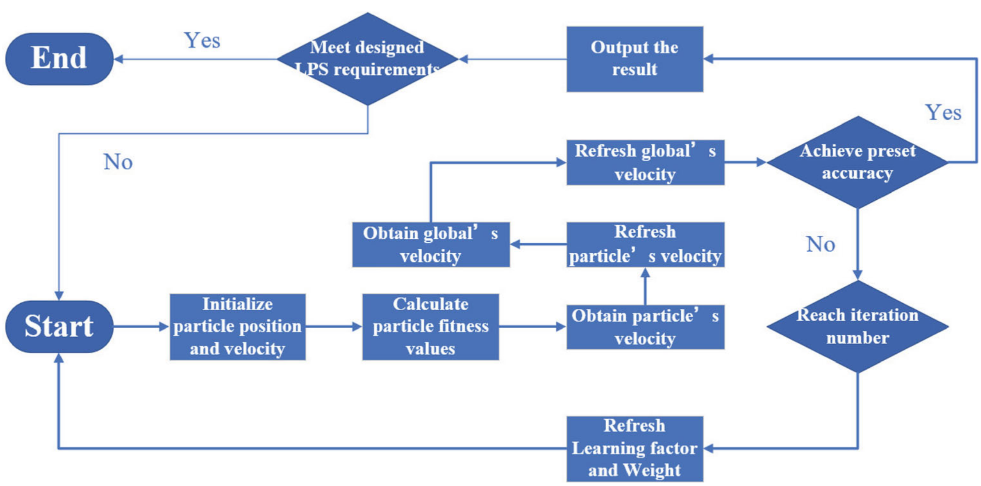

Figure 2. Algorithm process of IPSO.

optimal position $P_{indi}(w)$ and collective optimal position $P_{gro}(w)$, the meaning of i is the inertia factor, which is used to represent the influence of the original velocity on the next generation update velocity, and c_i represents the learning factor, which means that the particle velocity update is influenced by the position and the distance from the previous updated particle position. In the PSO, the setting of these three parameters greatly determines the execution efficiency and correctness of the algorithm. In this paper, a method of asynchronous automatic adjustment of the learning factor is applied to make the results obtained by the optimization algorithm more reasonable and correct [34], which makes the iteration curve more curved and the ability to find the optimal solution stronger.

$$\begin{aligned} c_1 &= c_{1.start} + (c_{1.end} - c_{1.start})\frac{G}{M}, c_{1.start} = 2.5, c_{1.end} = 0.5 \\ c_2 &= c_{2.start} + (c_{2.end} - c_{2.start})\frac{G}{M}, c_{2.start} = 0.5, c_{2.end} = 2.5 \end{aligned} \tag{9}$$

The learning factors c_1 and c_2 play a crucial role in determining the trajectory of optimization by influencing the individual particle experience and other particle experience, respectively, thereby enabling the exchange of information between particles. Large c_1 values tend to cause excessive local particle search, while large c_2 values cause premature convergence to locally optimal values. To address these issues, we adopt $c_{1.\text{start}} = 2.5$ and $c_{2.\text{start}} = 0.5$ at the initial stage of the algorithm search, emphasizing the 'individual independent consciousness' of particles to increase diversity in the group while minimizing the impact on the 'social consciousness part.' As the generation selection times increase, we increase the $c_{2.\text{end}}$ value of 2.5 and decrease the $c_{1.\text{end}}$ value of 0.5 to enhance particle convergence to the global optimum [35].

2.2.3. Evaluation factors for the performance of sensor

This section focuses on the design of a non-reciprocal sensor, for sensor performance evaluation when this study has a variety of methods, the most commonly used is through the *S*, *Q*, *FOM* and *DL*. The calculation formula is as follows [23].

$$S = \frac{\Delta f}{\Delta n} \tag{10}$$

$$Q = \frac{f_T}{FWHM} \tag{11}$$

$$FOM = \frac{S}{FWHM} \tag{12}$$

$$DL = \frac{f_T}{20 \times S \times Q} \tag{13}$$

where Δf and Δn stand for the amount of variation in frequency and RI, f_T represents the magnitude of the peak frequency, *FWHM* on behalf of the half-high frequency width of the absorption peak transmission peak. A well-designed sensor tends to have a significant *S*, *Q*, *FOM*, and a low *DL*. The values of these parameters depict the performance of sensing very visually.

3. Analysis and discussion

In practice, various measuring methods are employed for sensors, many of which utilize frequency modulation, similar to the approach used in this paper, to detect changes in the sensing parameter by the shifting of peak frequency. To achieve significant Q and S, we were very rigorous in the design of LPS. This requires that we have transmittance and absorptivity close to 1 over a certain frequency range, while at the same time trying to maintain their curve width. The function of the optimization algorithm is to set constraint conditions to find the optimal result locally. In this design structure, the basic structure is first built according to the physical principles, and then IPSO is used to optimize the thickness of each medium layer (d_1-d_7) adjustable medium RI (n_2, n_3, n_4, n_6), the periodic number of photon structure (p), working light intensity (It) and third-order nonlinear polarization (x_3). Constraint conditions conforming to the principle of physics were set for each parameter to be optimized, and appropriate population number and iteration times were selected for parameter optimization. Finally, very high results such as Table 1 and Figure 3(a) are obtained. And because of the setting of calculation accuracy, IPSO tends to the optimal results often cannot meet the requirements of industrial production. Therefore, further modification attempts are required to find an appropriate thickness and medium near the optimal result to complete the design of LPS.

Table 1. All parameters to be optimized.

Parameters to be optimized							
Parameter	range	unit	Optimization result	Parameter	range	unit	Optimization result
d_1	$10 \sim 10^3$	nm	64.7	n_2	$1 \sim 5$	None	2.62
d_2	$10 \sim 10^3$	nm	69.3	n_3	$1 \sim 5$	None	1.41
d_3	$10 \sim 10^3$	nm	31.5	n_4	$1 \sim 5$	None	1.09
d_4	$10 \sim 10^3$	nm	65.2	n_6	$-(1 \sim 5)$	None	-2.21
d_5	$10 \sim 10^3$	nm	321.3	p	$1 \sim 10$	pcs	3
d_6	$10 \sim 10^3$	nm	185.4	It	$0 \sim 10^6$	lx	7×10^5
d_7	$10 \sim 10^3$	nm	23.2	x_3	$1 \sim 5$	10^{-12}·C·m^2/V	1.14

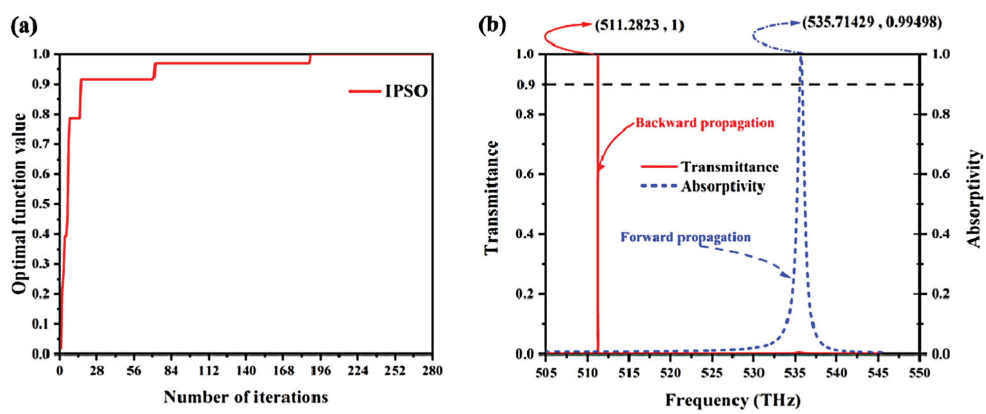

Figure 3. (a) The optimization results of IPSO. (b) The absorption peak and the transmittance peak inspired by OTS and defect layer.

In the case of the proposed LPS, a nonlinear dielectric layer is added to the proposed structure as a defect layer, which breaks the periodicity of the LPS and strengthens the electromagnetic wave to some extent. When the light comes in forward propagation, metallic Ag layers are added for activating the OTS, and a near-field electromagnetic wave is formed in the photonic band gap when the incident wave overlaps with the electric ions emitted from the metal surface. A better absorption peak is formed that could be attributed to the resonance to strengthen the enhancement effect of the local electric field when the frequency of the incident light is the same as the oscillation frequency of the electrons. When the light comes in backward propagation, the nonlinear medium is introduced as the defect, which generates the energy locality and forms a good transmission peak. The arrangement of the periodic structure allows the transmission of electromagnetic waves in the visible band resulting in a much more enhanced transmission of light through the dielectric layer. These two characteristics are well described in Figure 3(b). At $f = 535.7$ THz and $f = 511$ THz, an absorption peak with wide *FWHM* and a transmittance peak with narrow *FWHM* with a value up to 0.99498 and 1 are realized.

The sensor works by finding the relationship between the frequency and the analyte, thus converting the indistinct signal into a visible photoelectric signal. If the correlation coefficient of the object to be measured changes, the resonant frequency must produce a shift in a linear relationship. Sensors based on this principle have been shown to exhibit excellent sensing performance. With the high resolution and high-quality sensing performance shown in Figure 1, the sensor not only can measure common physical quantities of refractive index and thickness but also accurately measure C_G and C_{SCR}, reaching the measurement level of a biosensor.

3.1. Sensor performance for forward transmission

When the light propagates forward, this sensor is used for measurements of thickness and RI through the change of absorptivity and frequency, most notably for measurements of C_{SCR}. The details demonstrated in Figure 4(a) find that the absorption rate can reach above 0.9 in the required measurement range when the RI varies between $2.565 \sim 2.661$. RI modulation will influence the tweaks of wave vector and phase so that a shift in frequency forms an absorption peak. The high absorption rate is the basis for making frequency modulation sensors, and the high and stable absorption rate ensures the stable performance of the sensors.

This study uses the change in RI to represent the change in C_{SCR}, and Table 2 indicates their correspondence [27].

Based on the principle of frequency-modulated sensors, this study uses these measured SCR data to explore the linear relationship between $n = 2.565 \sim 2.661$ and resonant frequency, 520.4, 516.2, 512.6, 507.6, 504.9 and 503.9 THz. Figure 4(b,c) reveals that there is extremely high linearity among them. A possible explanation for this might be that the OTS effect is strongly influenced by the change in RI which affects the change in wave vector and associated phase, thus arousing a red-shift phenomenon in the absorption peak with increasing C_{SCR}. According to the linear fit, it can be derived to satisfy the functional relationship as Equation (14).

$$f_{SCR} = -172.1130n + 961.8466 \tag{14}$$

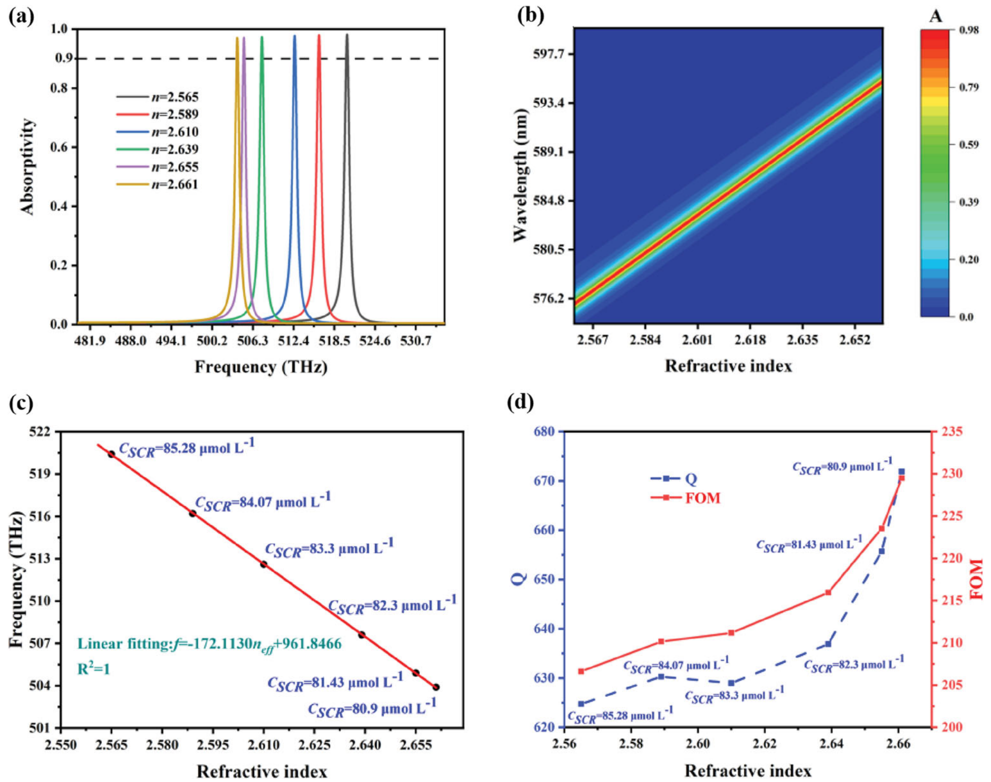

Figure 4. (a) Absorption peaks at different C_{SCR}. (b) The corresponding three-dimensional overhead plan for C_{SCR} sensing. (c) The linear relationship between the C_{SCR} and the resonance frequency. (d) *FOM* and *Q* values at different concentrations.

Table 2. Creatinine concentration (μmol L^{-1}) with attributed RI.

RI	Creatinine concentration (μmol L^{-1})
2.661	80.9
2.655	81.43
2.639	82.3
2.610	83.3
2.589	84.07
2.565	85.28

From Equation (14), through calculation, it can get that $S = 172.1130$ THz/RIU and the coefficient of determination reaches 1, approving the reliability of the sensor. By observing the line trend in Figure 4(c), it can be concluded that with the increase of RI from 2.565 to 2.661, the corresponding SCR concentration decreases from 85.28 to 80.9, and the corresponding peak frequency decreases from 520.4 THz to 503.9 THz. *Q* and *FOM* can be calculated by Equations (11) and (12). The different concentrations of *Q* and *FOM* are revealed in Figure 4(d), $Q = 651$, $FOM = 216$. The maximum values of *Q* and *FOM* are 672 and 230, respectively, and the minimum values are 625 and 207, respectively. It can be seen that the range of variation is 47 and 23, indicating that when the sensor changes the range of RI, that is, when the concentration of the object is measured, the sensor can always maintain a measurement level of the same quality. The average *DL* of 2.3163×10^{-4} can be calculated from Equation (13) which indicates that this sensor is sensitive and stable and can be used for fine measurements of SCR. *DL* is less than 10^{-4} indicating that the structure can guarantee certain accuracy and clarity when used as a sensor to measure biomass, which is a decisive factor for the practical production application of the sensor. Only a biosensor with qualified *DL* can really provide help for modern medical detection.

Next, similar to the principle of detecting C_{SCR}, this sensing structure can also be used to detect thickness when placing media with RI of 2.52 and 2.9 at the position of analytes 1 and 2. In Figure 5(a), the change in the cavity thickness of analyte 2 is from 80.5 to 84.5 nm, and the corresponding resonant frequency peaks are from 498.8 ~ 511.6 THz. In order to visualize the data, we plot Figure 5(b) which witnesses the exhaustive absorption properties of LPS under different wavelength and thickness conditions. And fit the expression linearly from Figure 5(c), $f = -3.2d + 769.18$, revealing that this sensor has $S = 3.2$ THz/nm, $R^2 = 0.99$. Unlike the RI sensor, the *S* of thickness sensor greater than 1 already has an excellent performance. Relevant formulas were used to obtain Figure 5(d) at several selected cavity thickness points which indicate that, average $Q = 868$ and $FOM = 500$.

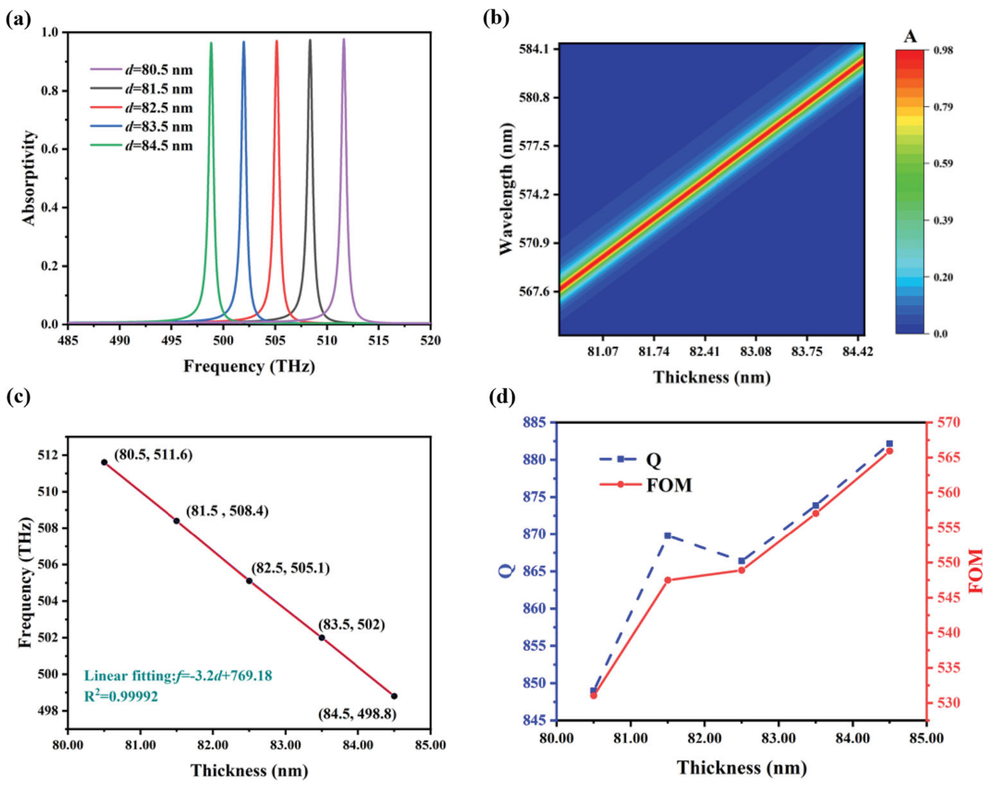

Figure 5. (a) Absorption characteristics of different cavity thicknesses at different frequency points. (b) Full wavelength absorption characteristics at different thicknesses. (c) Linear fitting over the thickness to be measured. (d) Sensing performance over a range of thickness variations.

Moreover, the Q value first rises from 849 to 870, then falls briefly to 866 and finally improves slowly to 882 at a slower rate. Corresponding to the changing trend of FOM, the rate of increase from 531 to 547 to 565 is first fast, then slow, and finally gentle, and the sensing performance is gradually improved with the increase of measurement thickness.

In Figure 6, we fill the test medium in analyte 1 and a normal medium with an RI of 2.9 with analyte 2. Similar simulations and calculations are carried out when the thickness of analyte 2 is adjusted to 31.5 nm. RIs are randomly selected as 2.52, 2.54, 2.56, 2.58 and 2.60. At frequencies 528.4, 524.8, 521.3, 517.8, and 514.3 THz, there is a simulated outstanding absorption corresponding to the electromagnetic wave passing through which is shown in Figure 6(a). According to the heat map in Figure 6(b), when the light incident from the front, the absorption characteristics only appear near the operating point relative to 5% of the whole range, which means that the sensing performance of different frequencies of electromagnetic waves is very different. By using LFR, a fitting method that selects the relationship between equally spaced points along the horizontal and vertical axes which gets the result, $f = -176n + 971.88$, is shown in Figure 6(c). S up to 176 THz/RIU, the R^2 up to 0.99, indicating the high quality of the linear fit, as RI increased from 2.52 to 2.60,

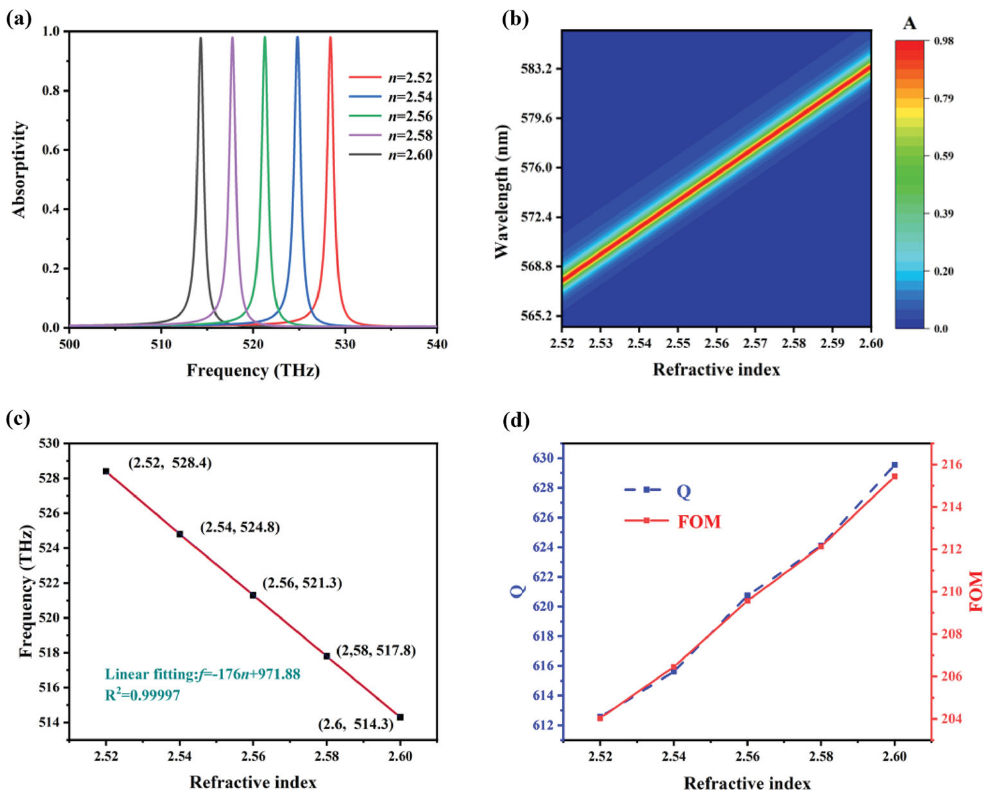

Figure 6. (a) Absorption peaks of each frequency point under different RI. (b) Absorption characteristics of each wavelength incident in RI range. (c) Linear relationship between frequency and range of RI measurement. (d) Variation of Q and FOM in RI measuring range.

the corresponding frequency decreased from 528.4 THz to 514.3 THz. The *Q* of 621 and the *FOM* of 210 are revealed in Figure 6(d) after accurate computational analysis. Within the measured range, $n = 2.60$ can obtain the maximum values of *Q* and *FOM*, 630 and 215, and it has a very stable growth trend in the transition from 514.3 THz to 528.4 THz.

3.2. Sensor performance for backward transmission

When the light propagates backward, the characteristics of absorptivity are not ideal and cannot be used as the basis of sensor design, but at this time, the transmittance is extremely excellent and can be made of transmittance sensor parts. To explore its transmission characteristics, it is found that when glucose solution is placed at analyte 2, the transmission could be observed to produce frequency point movement with the change of concentration, as shown in Figure 7(a).

With the change in the content of glucose, the increase or decrease of C_G value will cause a change in RI. In some previous studies, [23] the RI of C_G can be expressed as the formula Equation (15) [27].

$$n_G = 0.00011889C_G + 1.33230545 \tag{15}$$

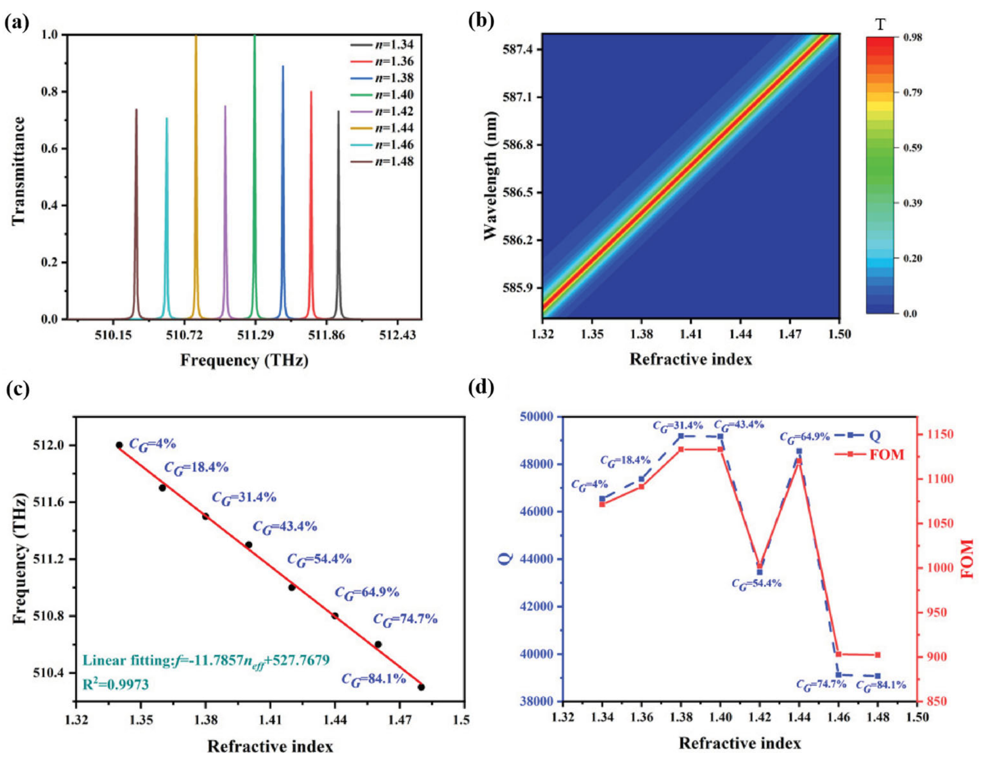

Figure 7. (a) Transmission peaks at different C_G. (b) The corresponding three-dimensional overhead plan for C_G sensing. (c) The relationship between C_G and resonance frequency. (d) *FOM* and *Q* values at different concentrations.

After knowing the relationship between RI and C_G, the relationship between them can be explored. In Figure 7(b), different frequencies are dotted with points with different transmittance which have enough physical properties to be used as a sensor. Achieve a wide range of concentration measurements for 4% ~ 84.1% in an aqueous solution of glucose within the n_G range of 1.34 ~ 1.48 is shown in Figure 7(c), indicating an excellent linear relationship.

$$f = -11.7857n + 527.7679 \tag{16}$$

From Equation (16), this study can obtain $S = 11.7857$ THz/RIU and $R^2 = 0.9973$. The RI detection range of 1.34 ~ 1.48 completely covered the RI belonging to solutions of normal glucose at the same concentration. Observed transmission peaks are mostly fine and short, with low FWHM on the surface, which is extremely friendly for the calculation of *Q* and *FOM*. Compared with the forward absorption peak, the *FWHM* is 9 ~ 10 times smaller, and the relative values of *Q* and *FOM* are also increased by 4 ~ 5 times. On the contrary, the *S* is affected and has a 145.9% decrease. In Figure 7(d), the details are shown, a relevant average data of $Q = 4.5 \times 10^4$, $FOM = 1.1 \times 10^3$, and $DL = 4.825 \times 10^{-5}$. Compared with the above, the *Q* and *FOM* values fluctuated more greatly, especially the sensing performance at $C_G = 54.4\%$ solution showed a short trough, $Q = 43{,}452$, FOM = 1002. Then, when C_G reaches 64.9%, *Q* and *FOM* reach the extreme value again, and finally drop sharply to $Q = 39{,}126$, $FOM = 903$, at 64.9% ~ 74.7%, it also reveals that the *DL* of the sensor changes from 4.4630×10^{-5} to 5.5364×10^{-5}. Therefore, a wide range of *Q* and *FOM* means that the relative accuracy of measurement will also change, which is helpful for distinguishing different concentrations of solutions.

In addition, it shows outstanding transmission properties when thickness varies. By changing the cavity size of analyte 2, after placing RI of 2.6 and 1.4 media at analytes 1 and 2, it can obtain significant transmittance peaks at different thicknesses with resonance frequency (see Figure 8(a)). The phase change of the electromagnetic field is induced by the nonlinear defect film. As a result, the transmittance of 498.8, 502.0, 505.1, 508.4, and 511.6 THz is higher than 0.8 at the frequency points. The theoretical basis of sensor fabrication for thickness measurement is presented in Figure 8(b), about 10% of the operating band has a suitable transmittance. Figure 8(c) reveals the strong linear relationship between them within the thickness of 25.8 nm ~ 26.2 nm, combined with the corresponding frequency relationship, $f = -5.4\text{d} + 676.5$. $S = 5.4$ THz/nm and the coefficient of determination is 0.99863, which is extremely strong and tends to be 100% coincidence, showing a strong linear relationship between frequency and transmittance. Figure 8(d) shows the superiority of the designed LPS and shows high sensing performance in thickness measurement, $Q = 24{,}205$, $FOM = 24{,}383$. In the range of 25.8 nm ~ 26.0 nm, $Q = 22{,}845 \sim 23{,}138$, $FOM = 22{,}964 \sim 23{,}306$, the growth potential of *Q* and *FOM* are smaller than that ($Q = 23{,}138 \sim 23{,}306$, $FOM = 23{,}306 \sim 25{,}862$) of 26.0 nm ~ 26.1 nm, which is close to the trend of 26.1 nm ~ 26.2 nm, $Q = 25{,}651 \sim 26{,}355$, $FOM = 25{,}862 \sim 26{,}601$.

A normal medium with $n = 2.6$ is placed at analyte 1 and the object to be measured at analyte 2, then the value of the thickness of analyte 2 is optimized to 31.5 nm. When LPS is used to measure changes in RI based on transmission characteristics. Figure 9 study the sensing characteristics of this improved metamorphic structure absorber by measuring the surrounding background transmission reaction of various RI from 1.353 to 1.393. An

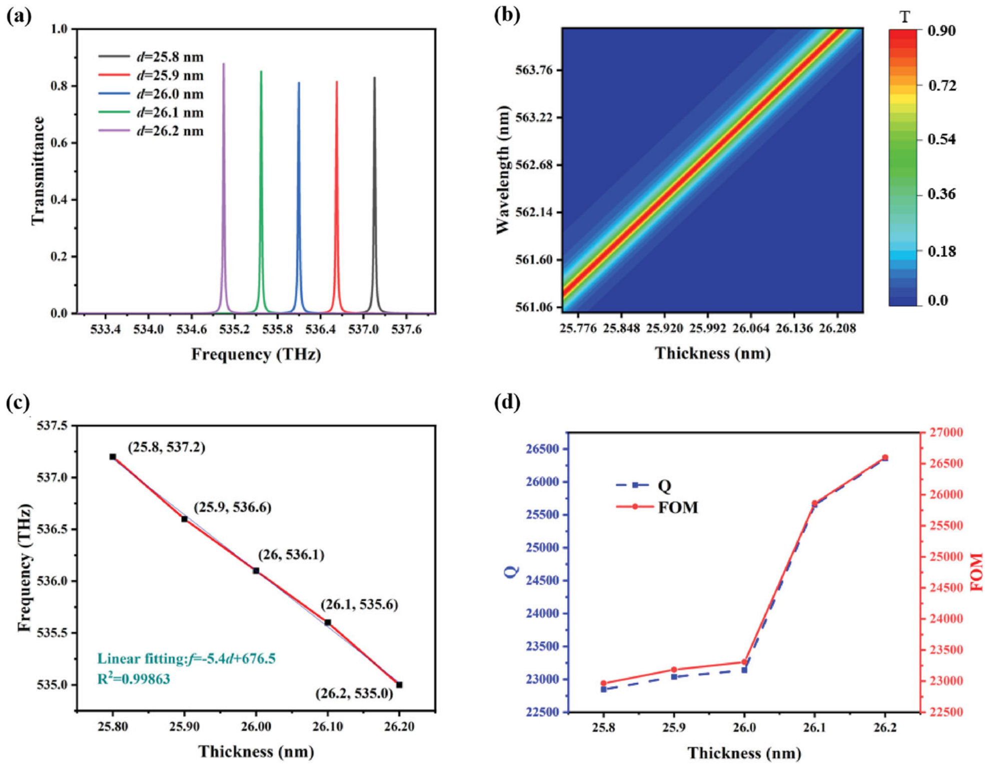

Figure 8. (a) Transmittance characteristics of different cavity thicknesses at different frequency points. (b) Full wavelength transmittance characteristics at different thicknesses. (c) Linear fitting over the thickness to be measured. (d) Sensing performance over a range of thickness variations.

apparent linear transmission peak redshift is observed in Figure 9(a) with an increase in RI measured around the material. By extracting relevant peak frequency data from Figure 9(a) and combining it with the corresponding measurement range of RI, their strong sensing characteristics and linear relationship can be explored, as shown in Figure 9(b,c). The fitting degree of $f = -10n + 525.33$ and $R^2 = 1$ can be obtained by calculation. In the range of 511.4 THz to 511.8 THz, there is an inverse correlation between the change of operating frequency and the corresponding measurement RI, which decreases from 1.393 to 1.353, indicating that the S is 10 THz/RIU. In order to a better and more comprehensive evaluation of sensor performance, $Q = 47{,}229$ and $FOM = 924$ are respectively obtained in Figure 9(d). According to the trend of the curve, the values of Q and FOM first increased at a certain rate, reached the maximum value of $Q = 49{,}680$, $FOM = 970$, then decreased at an approximate rate from $n = 1.363$ to $n = 1.383$, $Q = 49{,}680 \sim 45{,}792$, $FOM = 971 \sim 895$, and finally increased in reverse at $n = 1.383$($Q = 45{,}792$, $FOM = 895$). It shows the stability and superiority required for a good sensor.

The ability of a sensor to detect an analyte does not guarantee its selectivity for a specific concentration of the analyte, such as glucose or SCR. Typically, sensors rely on changes in the environment surrounding the sensor, which can result from factors like temperature, pressure, and the presence of different chemicals. To achieve specific detection of target analytes like glucose or SCR, it is necessary to use a sensing material that selectively interacts

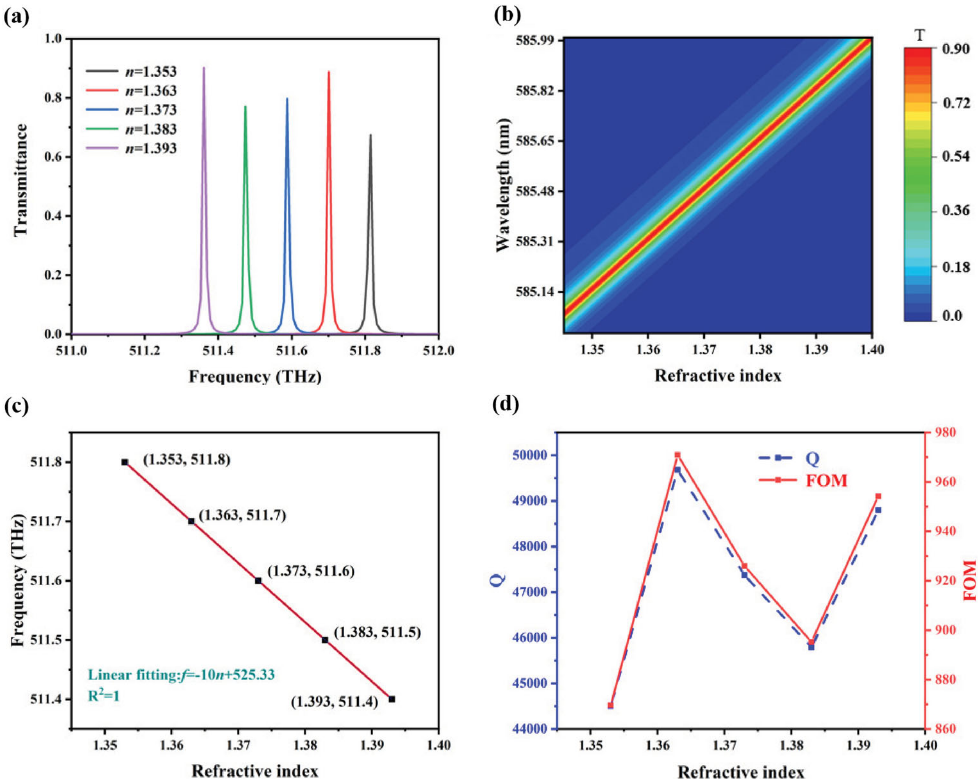

Figure 9. (a) Transmittance peaks of each frequency point under different RI. (b) Transmittance characteristics of each wavelength incident in RI range. (c) Linear relationship between frequency and range of RI measurement. (d) Variation of *Q* and *FOM* in RI measuring range.

with the analyte and causes a change in the RI of the medium. For instance, a sensor could use an enzyme that reacts specifically with glucose, leading to a proportional change in the RI of the solution [36]. Alternatively, sensors that combine refractive index measurements with other sensing mechanisms like surface plasmon resonance (SPR) or surface-enhanced Raman spectroscopy (SERS) can be used to achieve selective detection of target analytes [37,38]. These techniques rely on changes in optical properties that occur when a metal surface interacts with a specific analyte, making it possible to detect the analyte even in complex mixtures.

Last but not least, conventional sensors are often used only for single-physics measurements, dedicated to the fine measurement of a parameter. And it can only work with unidirectional incidence, which is extremely inefficient in practical applications. This paper proposes a multi-physics sensor, which can also be used for the measurement of different properties in different directions. Additionally, the sensor in this paper has excellent *Q*, *FOM*, and *DL* values, which are crucial for the fine measurement of solids and liquids. To highlight the features of the design of this paper, Table 3 is used for comparison. Combined with the sensor designed in this paper, the performance of the sensor is compared with that of the same type. While maintaining good *S*, *Q*, and *FOM*, three kinds of physical quantities can be measured at the same time.

Table 3. The performance of published literatures compared with this work.

Literature	Non-reciprocity	Multi-quantity measurement	Performance				
			Analyte	*S*	*Q*	*FOM*	*DL*
Ref. [36]	No	No	Blood serum	153	None	None	1.44×10^{-5}
Ref. [37]	No	No	Fat volume	51.3	7584	666	None
Ref. [38]	No	No	Gas	450	None	800	1.6×10^{-4}
Ref. [39]	No	No	Chemical analytes	268	None	1276	3.9×10^{-4}
Ref. [40]	No	No	Temperature	93.61	2506	None	None
Ref. [41]	No	Yes	Blood, Cancer cells	72.0906	18.971	None	None
Ref. [42]	No	No	Blood glucose	22	800	0.3865	None
Ref. [43]	No	No	RI	11	1420	407	None
Ref. [44]	No	No	CH_4	103	8.7	5.2	None
Ref. [45]	No	No	RI	4.78	2149	1477	None
			Forward				
This work	Yes	Yes	Analyte		SCR	RI	Thickness
			S		11.7857	10	5.4
			Q		45,000	47,228	24,205
			FOM		1100	924	24,383
			DL		4.825×10^{-5}	None	None
			Backward				
			Analyte		Glucose	RI	Thickness
			S		172	176	3.2
			Q		651	621	868
			FOM		216	210	500
			DL		2.316×10^{-4}	None	None

4. Conclusions

In summary, a non-reciprocal sensor that can measure both C_G and C_{SCR} is proposed in this paper, and TMM is utilized for data computation and analysis. When the light forward propagation, the analyte with a thickness of 69.3 nm is measured, and the corresponding values of *S*, *FOM*, *Q*, and *DL* are 172 THz/RIU, 217, 642, and 2.30×10^{-4}. When the light backward propagation, the analyte with a thickness of 31.5 nm is measured, and the corresponding values of *S*, *FOM*, *Q*, and *DL* are 12 THz/RIU, 1.1×10^3, 4.5×10^4, and 4.82×10^{-4}. The effect of the sensor on the sensing performance for the thickness and RI of common media is also briefly described. The advantages of these aspects mentioned in this paper are attributed to the fact that IPSO has a powerful multi-objective optimization function that can find the optimal solution for the sensor performance in several iterations. With the excellent sensing performance of such a simple and physical structure, it verifies the effectiveness of sensors that have a wide range of practical applications and IPSO will shine in many aspects of the optical field.

Disclosure statement

No potential conflict of interest was reported by the author(s).

References

[1] Yablonovitch E. Inhibited spontaneous emission in solid-state physics and electronics. Phys Rev Lett. 1987;58(20):2059. doi:10.1103/PhysRevLett.58.2059

[2] John S. Strong localization of photons in certain disordered dielectric superlattices. Phys Rev Lett. 1987;58(23):2486. doi:10.1103/PhysRevLett.58.2486

[3] Cheng C-C, Scherer A. Fabrication of photonic band-gap crystals. J Vac Sci Technol B Microelectron Nanom Struct Process Meas Phenom. 1995;13(6):2696–2700. doi:10.1116/1.588051

[4] Aly AH, Elsayed HA. Defect mode properties in a one-dimensional photonic crystal. Phys B. 2012;407(1):120–125. doi:10.1016/j.physb.2011.09.137

[5] Ayyanar N, Raja GT, Sharma M, et al. Photonic crystal fiber-based refractive index sensor for early detection of cancer. IEEE Sensors J. 2018;18(17):7093–7099. doi:10.1109/JSEN.2018.2854375

[6] Mollah MA, Islam SR, Yousufali M, et al. Plasmonic temperature sensor using D-shaped photonic crystal fiber. Results Phys. 2020;16:102966. doi:10.1016/j.rinp.2020.102966

[7] Wang J, Liu C, Wang F, et al. Surface plasmon resonance sensor based on coupling effects of dual photonic crystal fibers for low refractive indexes detection. Results Phys. 2020;18:103240. doi:10.1016/j.rinp.2020.103240

[8] Mohammed NA, Hamed MM, Khalaf AA. High-sensitivity ultra-quality factor and remarkable compact blood components biomedical sensor based on nanocavity coupled photonic crystal. Results Phys. 2019;14:102478. doi:10.1016/j.rinp.2019.102478

[9] Lv J, Ding D, Yang X, et al. Biomimetic chiral photonic crystals. Angew Chem Int Ed. 2019;58(23):7783–7787. doi:10.1002/anie.201903264

[10] Hou J, Li M, Song Y. Patterned colloidal photonic crystals. Angew Chem Int Ed. 2018;57(10): 2544–2553. doi:10.1002/anie.201704752

[11] Yagmurcukardes M, Qin Y, Ozen S, et al. Quantum properties and applications of 2D Janus crystals and their superlattices. Appl Phys Rev. 2020;7(1):011311. doi:10.1063/1.5135306

[12] Campuzano S, Gamella M, Serafín V, et al. Magnetic Janus particles for static and dynamic (bio) sensing. Magnetochemistry. 2019;5(3):47. doi:10.3390/magnetochemistry5030047

[13] Yi Y, Sanchez L, Gao Y. Janus particles for biological imaging and sensing. Analyst. 2016;141(12):3526–3539. doi:10.1039/C6AN00325G

[14] Depre C, Vanoverschelde J-LJ, Taegtmeyer H. Glucose for the heart. Circulation. 1999;99(4): 578–588. doi:10.1161/01.CIR.99.4.578

[15] Vafapour Z. Polarization-independent perfect optical metamaterial absorber as a glucose sensor in food industry applications. IEEE Trans Nanobioscience. 2019;18(4):622–627. doi:10.1109/TNB.2019.2929802

[16] Su Y, Guo H, Wang Z, et al. Au@ Cu_2O core-shell structure for high sensitive non-enzymatic glucose sensor. Sens Actuators B. 2018;255:2510–2519. doi:10.1016/j.snb.2017.09.056

[17] Warfel JD, Vandanmagsar B, Dubuisson OS, et al. Examination of carnitine palmitoyltransferase 1 abundance in white adipose tissue: implications in obesity research. Am J Phys Regul Integr Comp Physiol. 2017;312(5):R816–R820. doi:10.1152/ajpregu.00520.2016

[18] Wang Z, Zhang H, Yu W. Robust stability of Cohen–Grossberg neural networks via state transmission matrix. IEEE Trans Neural Netw. 2008;20(1):169–174. doi:10.1109/TNN.2008.2009119

[19] Hoefer WJ. The transmission-line matrix method-theory and applications. IEEE Trans Microwave Theory Tech. 1985;33(10):882–893. doi:10.1109/TMTT.1985.1133146

[20] Kennedy J, Eberhart R. Particle swarm optimization. Proceedings of ICNN'95-International Conference on Neural Networks, Perth, Vol. 4. IEEE. 1995.

[21] Wang D, Tan D, Liu L. Particle swarm optimization algorithm: an overview. Soft comput. 2018;22(2):387–408. doi:10.1007/s00500-016-2474-6

[22] Luo X, Pu M, Guo Y, et al. Electromagnetic architectures: structures, properties, functions and their intrinsic relationships in subwavelength optics and electromagnetics. Adv Photonics Res. 2021;2(10):2100023. doi:10.1002/adpr.202100023

[23] Wan BF, Wang QY, Peng HM, et al. A late-model optical biochemical sensor based on OTS for methane gas and glucose solution concentration detection. IEEE Sensors J. 2021;21(19):21465–21472. doi:10.1109/JSEN.2021.3103548

[24] Xiong C, Li H, Xu H, et al. Tunable ultra-narrowband multichannel filter based on plasmon photonic crystal and multimode cavity-coupled system. Opt Commun. 2020;458:124782. doi:10.1016/j.optcom.2019.124782

[25] Zhang J, Zhang R, Wang Y. Enhanced temperature sensing based on sub-threshold nonlinear spectra of one-dimensional photonic crystal with a Kerr defect layer. J Appl Phys. 2014;116(18):183104. doi:10.1063/1.4901470
[26] Xing F, Ge DZ, Hai FZ. Polarization rotator between the linear polarization and the circular polarization based on the layered photonic structure. Ann Phys. 2022;534(10):2200270. doi:10.1002/andp.202200270
[27] Aly AH, Mohamed D, Mohaseb MA, et al. Biophotonic sensor for the detection of creatinine concentration in blood serum based on 1D photonic crystal. RSC Adv. 2020;10(53):31765–31772. doi:10.1039/D0RA05448H
[28] Elsayed HA, Mehaney A. A new method for glucose detection using the one dimensional defective photonic crystals. Mater Res Express. 2018;6(3):036201. doi:10.1088/2053-1591/aaf3da
[29] Aly AH, Zaky ZA, Shalaby AS, et al. Theoretical study of hybrid multifunctional one-dimensional photonic crystal as a flexible blood sugar sensor. Phys Scr. 2020;95(3):035510. doi:10.1088/1402-4896/ab53f5
[30] Guo J, Zhang X, Fang Y, et al. Wideband low-frequency sound absorption by inhomogeneous multi-layer resonators with extended necks. Compos Struct. 2021;260:113538. doi:10.1016/j.compstruct.2020.113538
[31] Wang Y-H, Zhang H-F. Angular insensitive nonreciprocal ultrawide band absorption in plasma-embedded photonic crystals on improved particle swarm optimization algorithm. Chin Phys B. 2023;32(4):044207. doi:10.1088/1674-1056/ac8929
[32] Ghasemi F, Entezar SR, Razi S. Terahertz tunable photonic crystal optical filter containing graphene and nonlinear electro-optic polymer. Laser Phys. 2019;29(5):056201. doi:10.1088/1555-6611/ab05c2
[33] Zhu Y, Li G, Wang R, et al. Intelligent fault diagnosis of hydraulic piston pump combining improved LeNet-5 and PSO hyperparameter optimization. Appl Acoust. 2021;183:108336. doi:10.1016/j.apacoust.2021.108336
[34] Du W, Ding S. A survey on multi-agent deep reinforcement learning: from the perspective of challenges and applications. Artif Intell Rev. 2021;54(5):3215–3238. doi:10.1007/s10462-020-09938-y
[35] Chen Z, Yu L. A new structural damage detection strategy of hybrid PSO with Monte Carlo simulations and experimental verifications. Measurement. 2018;122:658–669. doi:10.1016/j.measurement.2018.01.068
[36] Koschinsky T, Heinemann L. Sensors for glucose monitoring: technical and clinical aspects. Diabetes Metab Res Rev. 2001;17(2):113–123. doi:10.1002/dmrr.188
[37] Subramanian P, Lesniewski A, Kaminska I. Lysozyme detection on aptamer functionalized graphene-coated SPR interfaces. Biosens Bioelectron. 2013;50:239–243. doi:10.1016/j.bios.2013.06.026
[38] Eremina OE, Sergeeva EA, Ferree MV. Dual-purpose SERS sensor for selective determination of polycyclic aromatic compounds via electron donor–acceptor traps. ACS Sensors. 2021;6(3):1057–1066. doi:10.1021/acssensors.0c02294
[39] Sriramprabha R, Sekar M, Revathi R, et al. Fe_2O_3/polyaniline supramolecular nanocomposite: a receptor free sensor platform for the quantitative determination of serum creatinine. Anal Chim Acta. 2020;1137:103–114. doi:10.1016/j.aca.2020.09.004
[40] Abohassan KM, Ashour HS, Abadla MM. A 1D binary photonic crystal sensor for detecting fat concentrations in commercial milk. RSC Adv. 2021;11(20):12058–12065. doi:10.1039/D1RA00955A
[41] Zaky ZA, Ahmed AM, Shalaby AS, et al. Refractive index gas sensor based on the Tamm state in a one-dimensional photonic crystal: theoretical optimization. Sci Rep. 2020;10(1):1–9. doi:10.1038/s41598-019-56847-4
[42] Elsayed HA, Mehaney A. Monitoring of soybean biodiesel based on the one-dimensional photonic crystals comprising porous silicon. Appl Nanosci. 2021;11(1):149–157. doi:10.1007/s13204-020-01579-5
[43] Bounaas F, Labbani A. High sensitivity temperature sensor based on photonic crystal resonant cavity. Prog Electromagn Res Lett. 2020;90:85–90. doi:10.2528/PIERL20010204

[44] Bijalwan A, Singh BK, Rastogi V. Analysis of one-dimensional photonic crystal based sensor for detection of blood plasma and cancer cells. Optik. 2021;226:165994. doi:10.1016/j.ijleo.2020.165994

[45] Chamoli SK, Singh SC, Guo C. Design of extremely sensitive refractive index sensors in infrared for blood glucose detection. IEEE Sensors J. 2020;20(9):4628–4634. doi:10.1109/JSEN.2020.2964715